Astron. Astrophys. 339, 759–772 (1998)

ASTRONOMY AND ASTROPHYSICS

The ultracompact H II region G45.45+0.06

A pearl necklace in the sky⋆,⋆⋆

M. Feldt[1], B. Stecklum[2], Th. Henning[1], T.L. Hayward[3], Th. Lehmann[1], and R. Klein[1]

[1] Astrophysikalisches Institut und Universitäts-Sternwarte, Schillergäßchen 2-3, D-07745 Jena, Germany
[2] Thüringer Landessternwarte, Sternwarte 5, D-07778 Tautenburg, Germany
[3] Center for Radiophysics and Space Research, Cornell University, Ithaca, NY 14853, USA

Received 13 March 1998 / Accepted 2 September 1998

Abstract. We present new imaging data on the ultracompact H II region G45.45+0.06 at near- and mid-infrared wavelengths. High-resolution data were taken in the H and K' bands using ESO's adaptive optics system ADONIS. The resulting images with a generic resolution of $0\farcs4$ for the first time allow the resolution of the object into several single point-like sources. Additionally, we present images obtained in the mid-infrared at 3.5, 10, and 12 μm. A Brγ image was obtained to serve as a measure for the extinction towards this region. We derive the physical properties of the point sources and show that some of them are young, massive stars. By combining our data with earlier VLA maps, we measure the extinction towards the region and discuss the history of the object. Finally, we conclude that G45.45+0.06 is a young OB cluster similar to the KL/BN Region in Orion and that sequential star formation is the reason for its present morphology.

Key words: methods: observational – H II regions – stars: formation – stars: early-type

1. Introduction

Ultracompact H II regions (UCH IIs) have long been known to be the postmark of the formation of massive stars. They are luminous, compact sources of infrared (IR) and radio continuum radiation caused by embedded stars of M $\geq 8M_{\odot}$ (Henning 1990, Churchwell 1991). The strong ultraviolet radiation of such stars produces dense, photo-ionized nebulae which are invisible at optical wavelengths (Wood & Churchwell 1989). Van Buren et al. (1990) suggested the so called bow-shock model for UCH IIs of cometary shape, where the appearance is explained by motion through the ambient matter. This model also provides a containment mechanism for the ionized region to account for the so called "lifetime problem" (Wood & Churchwell 1989, hereafter WC89). Hollenbach et al. (1994) published a hypothesis about UCH IIs being photo-evaporating circumstellar disks. This model also supplied an explanation for the longevity of the ultracompact phase (See also Yorke & Welz 1996). Even circumstellar disks and/or globules around lower mass stars that are being photo-evaporated by nearby massive stars ("proplyds", see, e.g., Churchwell et al. 1987; O'Dell & Wen 1994; McCullough et al. 1995) may appear as UCH IIs. Testi et al. (1997) and Molinari et al. (1998) suggest an evolutionary model for UCH IIs, where the radio emission might be suppressed during very early phases of massive star formation due to infall of surrounding dust. Recent observational studies suggest that for most of the models examples can be found which fit their implications (see Howard et al. 1994, Persi et al. 1997, Watson et al. 1998, Stecklum et al. 1998).

While observations in the near-infrared are common and needed because UCH IIs are deeply embedded in large amounts of dust, it is also mandatory to use as high a spatial resolution as possible. This not only enables us to detect weak point sources against the extended nebular emission, but also is necessary for a precise identification of such sources with counterparts at different wavelengths. Now that adaptive optics systems have become widely available, it is worthwhile to make a new attempt in this direction. This paper is intended to be the first in a series of publications of high-resolution observations of UCH IIs. The sources in this series where selected as bright sources from the WC89 sample with suitable ($m_V \leq 13$ mag) optical stars close ($\delta \leq 30''$) to them to serve as wavefront sensor for the adaptive optics system.

In addition, we are able to use this example to show that UCH IIs do not necessarily form around a single young massive star, but may also accompany the formation of a whole cluster of such stars. Indeed, we are able to compare G45.45+0.06 to the most well known OB cluster in our vicinity, the Orion Trapezium and the KL/BN region (named after Kleinmann & Low 1967 and Becklin & Neugebauer 1967).

In 1971, Wynn-Williams et al. made the first 6 and 11 cm aperture synthesis maps of the G45.5+0.1 complex using the Cambridge One Mile Telescope. They, and later Matthews et al. (1977), found G45.45+0.06 to be part of a cluster of three H II

Send offprint requests to: M. Feldt (e-mail: mfeldt@astro.uni-jena.de)

⋆ Based on observations collected at the European Southern Observatory, La Silla, Chile. Prop. ID:55.C-0647

⋆⋆ Based on observations collected at the DSAZ astronomical centre on Calar Alto, Spain

regions. The other two members of the cluster are G45.48+0.13 and G45.47+0.05[1]. Throughout the paper we will refer to the ultracompact H II region G45.45+0.06 itself as G45, while other regions are denoted separately by their galactic coordinates. The cluster members all share a similar radial velocity of approximately 58 kms^{-1} (Matthews et al. 1977). We adopt a distance of 6.6 kpc for G45, which was determined by Churchwell et al. (1990) after the Brand rotation curve (Brand 1986, Brand & Blitz 1993) from NH_3 measurements. Note that distance estimates for this source differ considerably in the literature but we consider direct line measurements and the Brand rotation curve the most reliable method for determining the distance. All authors resolve the near/far ambiguity to the near solution. The projected distances between the three regions range up to approximately 3 minutes of arc or 5.8 pc. Baud (1976) reported the discovery of a CO cloud coincident with the complex in both position and velocity.

G45 itself was classified as a cometary UCH II by WC89, after 6 cm VLA observations. From the measured radio flux, they determined the region to be ionized by a zero-age-main-sequence (ZAMS) star of spectral type O7.5. According to them, the IRAS fluxes suggest either an O4 star as the ionization source or a cluster with an O5.5 star as the brightest member. The cometary appearance was attributed to motion through ambient material. This motion provides at the same time a possible containment mechanism to explain the longevity of the ultracompact phase found for H II regions. However, Wilner et al. (1996) (hereafter W96) showed that the cometary structure of G45 is only a part of a larger shell structure, visible on their 3.6 cm VLA map. The shell structure was also observed at 6 cm by Garay et al. (1993). W96 also have detected clumps in the surrounding cloud, traced by HCO^+(1-0) emission. They speculate about the expansion of G45 having provided the trigger for the more recent star formation in G45.47+0.05. Since all their clumps contain sufficient mass ($20 - 100\,M_\odot$) to form massive stars, they speculate about the whole region being in an early stage of the formation of an OB star cluster. Mooney et al. (1995) used 1.3 mm continuum observations to determine the total mass of G45 to be $5000\,M_\odot$.

In this paper we present the result of our infrared imaging campaign of G45. This campaign included high-resolution adaptive optics imaging in the near-infrared (NIR, H- and K'-band) as well "conventional" NIR imaging (Brγ) and imaging in the thermal infrared (MIR, L- and N-band). The very high resolution of the AO images reveals 15 compact sources inside G45. The wide wavelength range of our observations shows that all the sources detected are deeply embedded, some of them invisible even in the NIR. In Sect. 2, we briefly describe our observations and the follow-up data reduction techniques used, while the results are presented in Sect. 3. In the discussion (Sect. 4), we argue that the point sources are deeply embedded, young massive stars. This is also verified by using the Brγ image as an additional estimator for the extinction towards G45. From a multi-wavelength comparison between the morphological structures in the different images starting with our NIR images and ending with VLA data taken at cm wavelengths, we speculate about the history of the object and the possibility of triggered star formation.

[1] The nomenclature of the sources is based on their galactic coordinates which may differ by $\pm 0.01^\circ$ in the literature.

2. Observations and data reduction

2.1. Adaptive optics imaging

G45 was observed in August 1995. ESO's adaptive optics system ADONIS (Beuzit et al. 1994) was used at the 3.6 m telescope on La Silla/Chile to obtain high-resolution images in the H and K' bands. In K', a mosaic of two frames was made that resulted in a total integration time of 400 s in the image centre.

During the observations, the seeing was $1''$, the high-order adaptive optics correction improved the full-width half-maximum (FWHM) of the point spread function (PSF) to $0\farcs4$. The integration time for the H image was 300 s. All frames were subject to standard bad-pixel removal, flat fielding, and dark-frame subtraction processes before being combined in the resulting images. For better identification of the point sources, part of the K' image was deconvolved with the point source located at position ($0''$,$0''$) using 200 iterations of a slightly modified maximum-likelihood deconvolution algorithm. The modification concerns the last step of each iteration, where the re-convolution is done with a narrower Gaussian instead of the original point-spread-function as described in Lucy (1974). This results in a better resolution of close point sources. Photometric calibration for the NIR images was obtained by calibrating the fluxes in the images using separate images of the UKIRT standard Y 4338.

2.2. MIR imaging

Three mid-infrared images were obtained. The first one was taken using SpectroCam-10 (Hayward et al. 1993) at the 200-inch Hale Telescope of the Palomar Observatory[2]. The filter effective wavelength was 11.7 μm with $\Delta\lambda = 1\,\mu$m. A 5 frame mosaic was combined into the image, the average on-source time at each pixel is 20 s. The star αLyr served as a standard for flux calibration. This image will be referred to as the 12 μm image in the discussion. The second image was taken using MANIAC (Böker et al. 1997) at ESO's 2.2 m telescope on La Silla/Chile. MANIAC's N-band filter was used with $\lambda_{center} = 10.5\,\mu$m and $\Delta\lambda = 5\,\mu$m. The total integration time sums up to 1135 s for the frames that were combined into the image. Photometric calibration was obtained by observing the standard stars γ Aqu, α Ser, and δ^2 Gru. This will be our 10 μm or N image.

A third MIR image was obtained in the L-band ($\lambda_{center} = 3.8\,\mu$m, $\Delta\lambda = 0.6\,\mu$m). The new MIR-Camera TC-MIRC (Robberto et al. 1994) was used at the 1.5 m TIRGO telescope

[2] Observations at the Palomar Observatory were made as part of a continuing collaborative agreement between the California Institute of Technology, Cornell University, and the Jet Propulsion Laboratory.

Table 1. Summary of observations

Date	λ	Tel./Instr.	FOV[a]	PSF FWHM	Ref. Star[b]	Limiting Mag.
1992 Aug	11.7 μm ($\Delta\lambda = 1\mu$m)	200" Hale /SpectroCam10	16.″2	1.″1	αLyr (0.00)	9.3[c]
1995 Aug	2.15 μm (K')	ESO 3.6 m/ADONIS	12.″8	0.″4[d]	Y4338 (5.42)	18.4
1995 Aug	1.64 μm (H)	ESO 3.6 m/ADONIS	12.″8	0.″5[d]	Y4338 (5.68)	20.0
1997 Jul	10.5 μm (N)	ESO 2.2 m/MANIAC	21.″8	1.″3	γAqu (0.78)	10.7
1997 Jul	2.166 μm (Brγ)	CA 2.2 m/MAGIC	164.″0	1.″1	GL748 (6.30)	14.6
1997 Oct	3.5 μm (L)	TIRGO 1.5 m/TC-MIRC	70.″4	2.″5	HD203856 (6.84)	14.5

[a] Field of view for single frames
[b] With brightness given in magnitudes for the observed wavelength
[c] Derived from background noise for point sources with given PSF
[d] Seeing was 1.″0 during the observations, the resolution is improved by the adaptive optics correction

on Gornergrat/Switzerland. The total integration time for this image was 600 s. Photometric calibration was achieved by observing the standard star HD203856. This image will be referred to as 3.8 μm or L image.

2.3. Narrow band imaging

The Brγ image was taken using BLUE-MAGIC (Herbst et al. 1993) at the 2.2 m telescope on Calar Alto/Spain which belongs to the German-Spanish Astronomical Centre. One image was taken using the Brγ ($\lambda = 2.166\,\mu$m, $\Delta\lambda = 0.022\,\mu$m), another one with the adjacent continuum filter ($\lambda = 2.22\,\mu$m, $\Delta\lambda$ = $0.022\,\mu$m). The total integration time for each of these images was 900 s. Photometric calibration was achieved by using the standard star GL748. Its magnitudes at the wavelengths of the continuum and the Brγ filter were derived by interpolating its known spectral energy distribution, assuming a featureless spectrum. After subtraction of the continuum, it turned out that the residual total fluxes in the stellar PSFs in the image were below the sky sigma level, so no further corrections were applied.

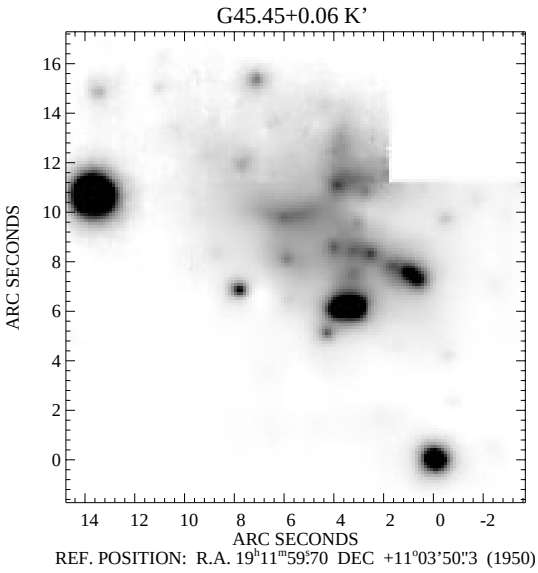

Fig. 1. K' image of G45.

2.4. The astrometric reference frame

When drawing conclusions on the nature of a certain object, a great deal of the information is taken from the comparison of its structural appearances at different wavelengths. Apart from other issues like the different beam sizes for each observation, it is crucial to establish a common astrometric reference frame for all images. This is especially difficult when one tries to match images of 0.″2 resolution like our deconvolved K' image and the 6 cm VLA maps from WC89. We adopted a two-way strategy to build our reference frame: First, the position of the wavefront calibrator which is visible in the K' image at position (+14″,+11″) (see Fig. 1) was taken from the digitized sky survey. The image was then calibrated using the known scale of 50 milliseconds of arc per pixel. This tied the NIR reference frame to the digitized sky survey. Secondly, the astrometry for the Brγ image taken with MAGIC was obtained by optimizing the cross-correlation with the 6 cm VLA image, the latter one being smoothed to the same resolution before the procedure. As the Brγ image contains the same stars as the K' image (before continuum subtraction, of course), we were able to check the two astrometric frames against each other. It turned out that the deviations between them were below 0.″2. This indicates that all larger offsets are indeed real. The method of optimizing cross-correlation was also applied to tie the 10μm image to the reference frame. Before optimizing the cross-correlation between the images, a mask was applied that blanked everything except the ionization front. The reference frames of the 12 and 3.5 μm images were chosen to make the MIR point-source at position (+3″,+10.″5) appear at identical positions in all MIR images.

2.5. Photometry

Photometry of the point sources detected in the AO images was performed in an aperture of 0.″5 diameter because of the

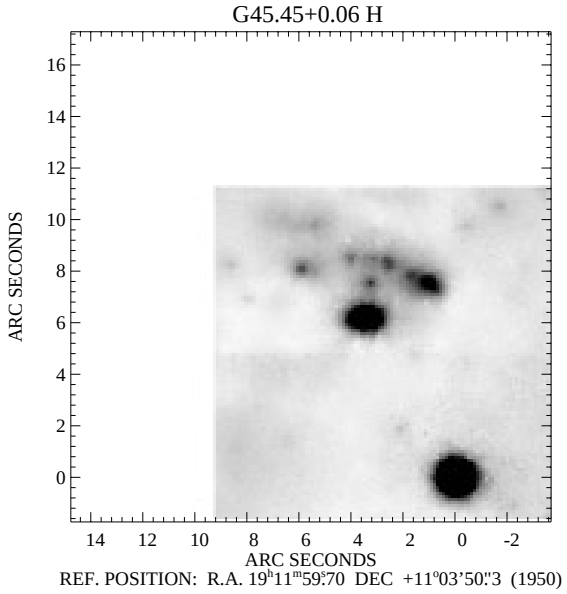

Fig. 2. H image of G45.

crowdedness of the field. Due to the non-Gaussian shape of the AO-corrected PSF, an aperture correction of 0.95 mag in K' and 1.23 mag in H was applied to account for flux outside the aperture. This correction was determined using sources at the reference position as well as a and b (in H, a is not visible). Background subtraction was achieved by subtracting the mean value of six sky measurements around the corresponding source using the same aperture to account for the varying background. The 3σ detection limit in the K'-image is $m_{K'} = 17.5$ mag, in the H-image it is $m_H = 18.5$ mag, both derived from the sky noise. Photometric accuracy is generally better than ± 0.1 mag. Photometry of the MIR images was done using an aperture of 4″ (2.″75 at 3.5 μm) diameter. Background subtraction was achieved in the same way as in K' and H. The accuracy of the photometric measurements in these images amounts to approximately 7% of the flux level or 0.1 magnitudes at most. The total source flux was determined in these images as well as in the K' image by applying an aperture of 11″ diameter.

2.6. A word on image filtering

All images presented as results from our imaging campaign were subject to filtering with the multi-scale maximum entropy method described by Pantin & Starck (1995). This method uses a wavelet decomposition to detect and remove the noise from an image. The K' band image was also subject to this kind of filtering before the deconvolution was applied. However, all this filtering was done solely for illustrative purposes. All photometric and mathematical operations described throughout the paper were performed on the "raw" data, before filtering or deconvolution. It should be stressed that all features discussed in the text can be found in the raw data. Therefore, we are certain not to describe any filtering artifacts whatsoever!

3. Results

In this section we will present the images resulting from our multi-wavelength campaign and the basic parameters that were derived from them. Conclusions drawn from these parameters and comments on specific features visible in the images can be found in in the next section.

The resulting K'-band image is shown in Fig. 1. All figures use the star at (0″,0″) as positional reference. The wavefront calibrator is visible at position (+14″,+11″). G45 itself is at and west of the image centre. The brightest source belonging to G45 is the strong one at position (+3.″5,+6) which looks elongated in east-west direction because it actually consists of three close point sources. North of this triple source several unresolved sources are grouped along an arc opening to the south, much like pearls on the chain of a necklace. In Fig. 3, it turns out that part of this arc coincides with the ionization front. Several point sources are also visible above the chain, one of these is especially interesting: The one at position (+3″,+10.″5) appears as a very strong mid-infrared source in the corresponding images. Immediately east of that one at position (+4″,+10.″8) is a source with an extended structure attached to it. Another source of this kind can be seen to the southeast at position (+6″,+9.″8). A preliminary reduced colour version of this image can be found in Stecklum et al. (1995).

Fig. 2 shows the H-band image which is of quite similar structure. Albeit it shows only the southwestern portion of the K'-band image, the same structure of pearl-chain, strong source below, and positional reference is visible.

Fig. 3 shows the deconvolved version of the K'-band image. Only the portion common to both the K'- and H-band images was deconvolved. The point sources are now clearly visible and have been denoted by letters for identification. From the superimposed VLA map by WC89 it becomes clear, that the chain-like structure also follows the ionization front. The strong source below the arc of the chain is now clearly resolved into three single sources labelled l to n.

The result of our Brγ imaging can be found in Fig. 4. It shows an overview map of the region, taken from the continuum narrow-band image at 2.22 μm. Superimposed are the contours of the continuum subtracted line emission. Since the image was taken with "conventional" NIR imaging, the resolution is much lower than in the K' and H images. However, due to the larger field of view we gain valuable information on the overall structure of G45. It can be seen that the whole ionized region has a structure like a horseshoe opening to the southeast with an extra structure pointing north from G45. Taking the weak 3.6 cm emission in the southeastern corner into account, the horseshoe completes itself to a shell-like structure with a diameter of approximately 40″. The 40″diameter corresponds to a linear size of 1.3 pc.

The results of our MIR imaging can be seen in Fig. 5. Fig. 5a shows the 3.5 μm image, Fig. 5b the 10 μm image and part c the 12 μm image. The contour lines represent the 6 cm VLA map obtained by WC89, the crosses denote the point sources found in the near-infrared images. Two point sources can be seen in

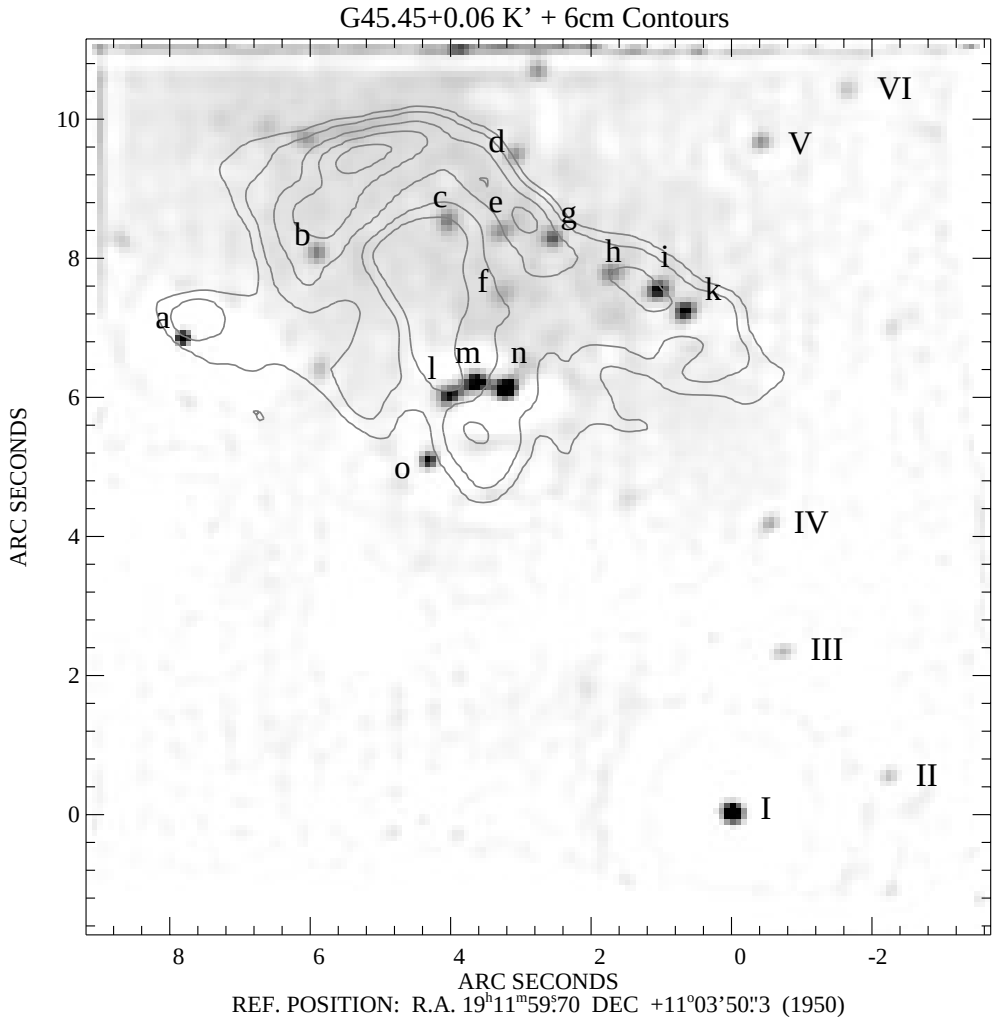

Fig. 3. Deconvolved K' image of G45.45+0.06. The image from Fig. 1 was subject to 200 iterations of a damped Richardson-Lucy deconvolution. The contours represent a 6 cm VLA image from WC89.

all images, a strong one at position (+3″,+10.″5) (This will be referred to as *MIR1*) and another one at position (+3.″8,+4.″8) (*MIR2*).

Table 2 compiles the results of the photometric and positional measurements of the point-like sources visible in the K' band image. Brightnesses were measured whenever possible in K' and H. The astrometric positions were determined in K' by centering an aperture of 0.5″ diameter on the star and computing the mean of all pixels weighted on their brightness (an analogue to the conventional "centre of mass"). The identification letters (IDs) of the sources are the same as in Fig. 3. Sources inside the VLA map are denoted by characters from a to o, other point sources in our images by roman numbers.

Fig. 6 shows the spectral energy distribution of G45. The upper line is the integrated flux of the whole region. Our contributions to this curve (marked by the triangle symbols) were measured in an aperture of 11″diameter. This explains the step between our data and the IRAS data, which were measured in a much larger aperture. The steep rise in the NIR is followed by a decline longwards of 100 μm and the typical flat radio plateau with a spectral index of ≈ 0.1 longwards of 1 cm. The latter one is caused by free-free emission from the ionized gas. The lower curve represents only the source *MIR1*, measured in an 0.″5 diameter aperture in K', 2.″75 in L and 4″ at 10 μm. This curve shows, that source *MIR1* is contributing up to 10% of the total flux of G45 (including *MIR1*!) at infrared wavelengths. In a new VLA map of the source taken at 1.3 cm by Hofner et al. (1998), this source also stands out as a single point source and contributes a significant portion of the total radio flux. However, as the VLA observation was pointed at G45.47+0.05, G45 lies only at the rim of the primary beam where the signal-to-noise ratio is not sufficient to measure the flux contribution from the point source *MIR1* reliably.

4. Discussion

In this section, we try to derive the nature of G45 from the measured properties. From the colour information, we determine the spectral types of the point sources and argue that G45 is a cluster of young, massive stars. To be able to do this, we first have to measure the extinction towards these sources. This information is extracted from a comparison between our Brγ data as well as the 6 cm and 3.6 cm VLA data by WC89 and W96.

Going further, we speculate on the cause of the ionization and the possible scenarios of the star formation sequence in the

Table 2. Point sources in G45

ID[a]	K' (mag)	H (mag)	R.A. (1950)	DEC. (1950)
a	13.6	–[b]	$19^h12^m00^s.24$	$+11°03'57''.0$
b	14.2	15.6	$19^h12^m00^s.11$	$+11°03'58''.2$
c	13.8	15.9	$19^h11^m59^s.98$	$+11°03'58''.6$
d	14.2	–	$19^h11^m59^s.92$	$+11°03'59''.6$
e	13.8	15.7	$19^h11^m59^s.93$	$+11°03'58''.6$
f	13.9	15.5	$19^h11^m59^s.93$	$+11°03'57''.6$
g	13.7	15.3	$19^h11^m59^s.89$	$+11°03'58''.4$
h	13.8	15.2	$19^h11^m59^s.82$	$+11°03'58''.0$
i	13.2	14.7	$19^h11^m59^s.78$	$+11°03'57''.7$
k	13.2	15.3	$19^h11^m59^s.75$	$+11°03'57''.4$
l	–[c]	–	$19^h11^m59^s.98$	$+11°03'56''.2$
m	–[c]	–	$19^h11^m59^s.95$	$+11°03'56''.3$
n	–[c]	–	$19^h11^m59^s.92$	$+11°03'56''.3$
o	14.1	–	$19^h12^m00^s.00$	$+11°03'55''.3$
I	12.3	11.9	$19^h11^m59^s.70$	$+11°03'50''.3$
II	–[c]	–	$19^h11^m59^s.55$	$+11°03'50''.8$
III	16.6	–	$19^h11^m59^s.65$	$+11°03'52''.6$
IV	16.3	–	$19^h11^m59^s.67$	$+11°03'54''.4$
V	15.8	17.7	$19^h11^m59^s.68$	$+11°03'59''.8$
VI	17.6	17.3	$19^h11^m59^s.68$	$+11°03'59''.8$
MIR1	14.5	–	$19^h11^m59^s.9$	$+11°04'01''$

[a] Source labelling is the same as in Fig. 3, except for source *MIR1*, which is explained in the text.
[b] Not all point sources are detected in H.
[c] Photometry not possible in un-deconvolved image.

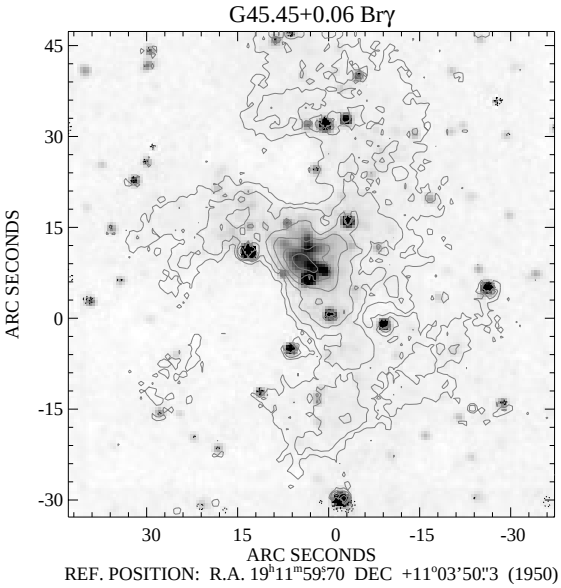

Fig. 4. Brγ image of G45. The superimposed contours denote the continuum-subtracted line emission with contour levels set at $[-2, -1, -0.5, 0.5, 1, 2, 4, 8, 16, 32, 64] \times 0.24$ mJy/$\Box''$. The gray scale image is the corresponding continuum image (2.22 μm). Negative contours are dotted, they indicate artifacts from imperfect alignment during continuum subtraction.

cluster. In the end, we will draw a parallel to the Orion Trapezium and KL/BN regions by comparing parts of G45 with these regions. Although the Orion region is not in the UCH II phase any more and the emission measure is two orders of magnitude lower there (Felli et al. 1993), we can still compare the dense cluster of stars at G45's southern edge with the Trapezium cluster and the larger part of it with the KL region. Perhaps *MIR1* may even be an analogue to the BN object.

4.1. The extinction towards G45

To derive the extinction towards the embedded sources in G45, we use the 6 cm map to determine the emission measure and thus the expected Brγ emission. By comparing this prediction to the actually measured Brγ flux, we get the extinction towards G45 at the line's wavelength. This extinction is assumed to be constant throughout the K' band. Several difficulties arise during this process: The 6 cm VLA map was obtained in the A configuration of the VLA. This means, the largest visible structures in the map can be of order $10''$ across (WC89). From Fig. 4, as well as from the 3.6 cm map from W96 we learn however, that weak emission extends over a much larger area. Thus, we have to account for possible losses of flux in the 6 cm map. This is done by predicting the 6 cm flux from the 3.6 cm flux assuming a spectral index of 0.1. By comparing this to the real 6 cm map, smoothed to the same resolution, we get a map of fraction of missing flux, which is shown as contours in Fig. 7b. At the location of G45, the fraction of flux that is missing generally is of the order of 50%, i.e. we see only half of the flux we should in the 6 cm map. This means that by predicting the Brγ flux from this map alone leads to a serious underestimation and thus the comparison to the measured flux also underestimates the extinction. On the other hand, we can not use the 3.6 cm map to predict the Brγ emission, because the resolution of this map is too low and we would thus average the extinction over too large an area. As the Brγ image shows that most of the emission comes from a very small area, the measured extinction would again be largely underestimated by using the 3.6 cm map alone. To get out of this dilemma, we tried to correct the 6 cm map for the missing flux by using the now known fraction of missing flux derived above. The resulting corrected 6 cm map is then used to predict the Brγ flux and thereby determine the extinction in a way outlined in Watson et al. (1998): First, we convolve the corrected 6 cm image to match the resolution of our Brγ image. Then we use the familiar expressions to determine the brightness temperature T_b at each point of the corrected 6 cm map (all units are cgs):

$$T_b = \frac{S_\nu 10^{-29} c^2}{2\nu^2 k \Omega_b} \quad (1)$$

(e.g. Rohlfs 1990).

In this formula, Ω_b is the solid angle of the synthesized beam, and $\frac{S_\nu}{\Omega_b}$ is the flux density in mJy·beam^{-1}, both after the convolution to the new resolution! The quantity c denotes the speed of light, k is the Boltzmann constant and ν the frequency at which the data were taken. We combine this with

$$T_b = T_e(1 - e^{-\tau}) \quad (2)$$

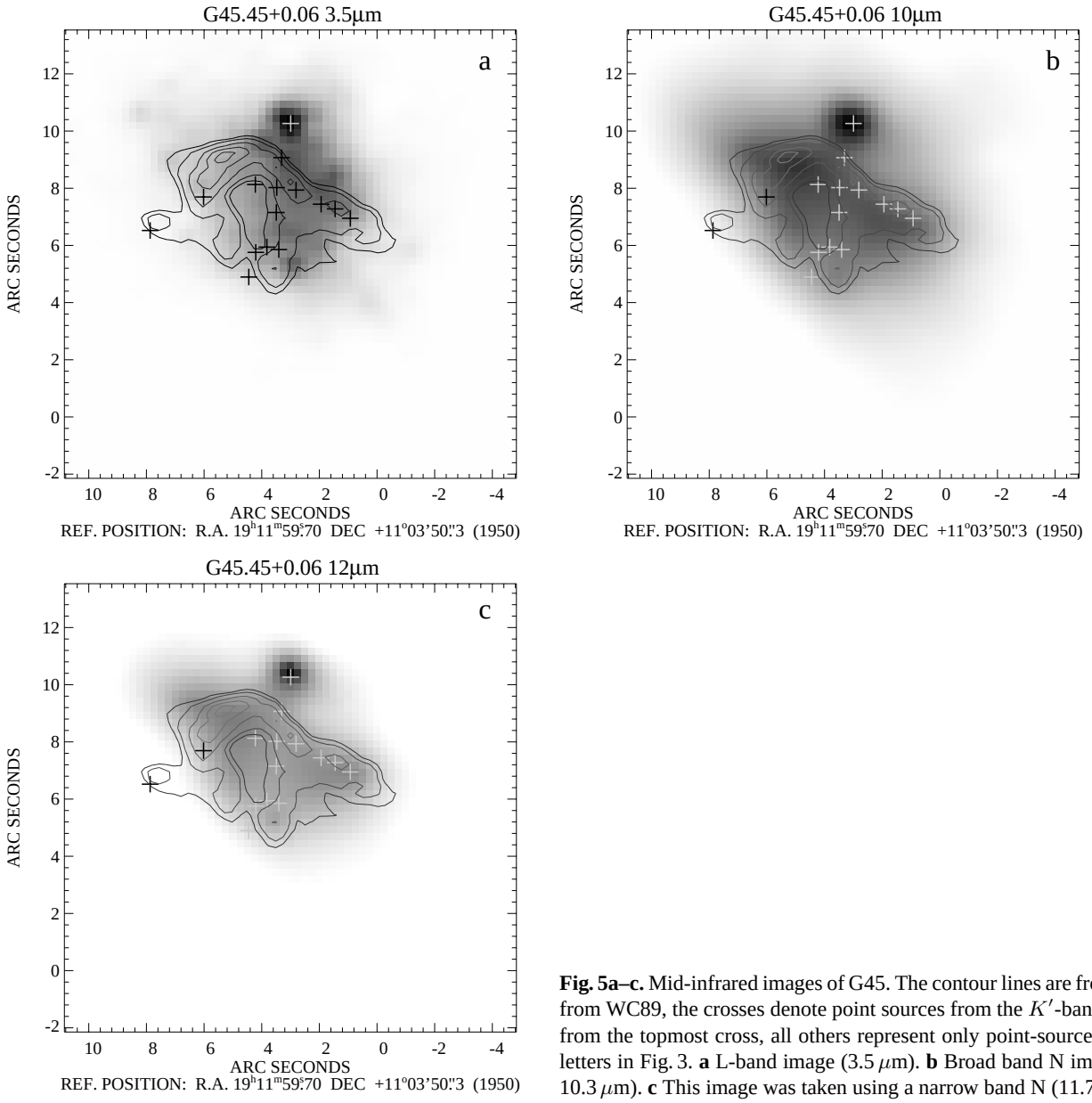

Fig. 5a–c. Mid-infrared images of G45. The contour lines are from a radio map from WC89, the crosses denote point sources from the K'-band image. Apart from the topmost cross, all others represent only point-sources denoted with letters in Fig. 3. **a** L-band image (3.5 μm). **b** Broad band N image (centred at 10.3 μm). **c** This image was taken using a narrow band N (11.7 μm) filter.

and

$$\tau = 2.11 \times 10^{-1} T_e^{-1.35} \nu^{-2.1} EM a(\nu, T) \quad (3)$$

(Mezger & Henderson 1967),

where τ is the optical depth, T_e the electron temperature, ν the observed frequency, EM the emission measure, and a a correction factor of order 1 (Mezger & Henderson 1967). The combination gives the emission measure as

$$EM = 4.72 a^{-1} T_e^{1.35} \nu^{2.1} \ln\left(\frac{T_e}{T_e - T_b}\right). \quad (4)$$

Once we have determined the emission measure, we can calculate the measured Brγ flux after Osterbrock (1989) to be:

$$S_{\mathrm{Br}\gamma} = 0.9 h \nu_{\mathrm{Br}\gamma} \alpha^{\mathrm{eff}}_{\mathrm{Br}\gamma} \frac{\Omega_{\mathrm{Br}_\gamma}}{4\pi} EM \quad (5)$$

The factor of 0.9 represents the assumption that only 90% of the nebula consists of Hydrogen, the rest of Helium. For $\alpha^{\mathrm{eff}}_{\mathrm{Br}\gamma}$, which comprises the transition coefficients and the level populations via a temperature dependency, Hummer & Storey (1987) give

$$\alpha^{\mathrm{eff}}_{\mathrm{Br}\gamma} = 6.48 \times 10^{-11} T_e^{-1.06}. \quad (6)$$

The solid angle $\Omega_{\mathrm{Br}\gamma}$ is now the pixel size of the Brγ image.

The emission measure computed from the corrected radio flux has its maximum at 21.7×10^7 pc·cm^{-6} with a mean value of 3.0×10^7 pc·cm^{-6}, assuming the Brγ beam of 2.8×10^{-11} sr to be uniformly filled with 10^4 K gas.

The result of the whole procedure can be seen in Fig. 7. Fig. 7a shows the measured Brγ image with the continuum emission already subtracted. Some remnants of bright stars can be

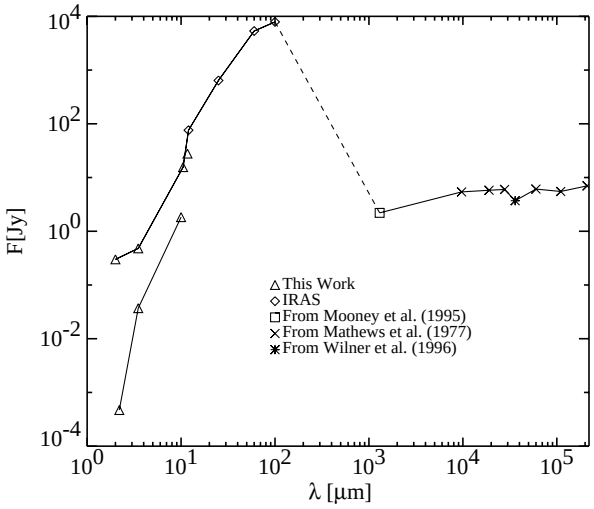

Fig. 6. Spectral energy distribution of G45. The upper line is the integrated flux from the whole UCHII region, the lower one is source *MIR1* alone. The dashed line denotes an obvious gap in the SED where no observations have been made up to now.

seen which are due to imperfect alignment of the line- and the continuum image during subtraction. Fig. 7b gives the prediction as computed from the 6 cm image. The ratio of the predicted and the measured Brγ flux yields the extinction towards the nebula in Brγ. We assume the resulting value to be constant over the K'-band and consequently use it as K' extinction. Also shown in this part of the figure are the contours denoting the missing 6 cm-flux, which show that at the location of G45 the missing flux fraction is about 50% with little variation across the region of interest. Fig. 7c shows the resulting extinction map superimposed as contours on the deconvolved K'-image. The extinction was calculated only in areas where both the flux in the 6 cm map and in the Brγ image was above 1.5 times the corresponding sky sigma level. In Fig. 7c, this means that outside the contours we do not have any information on the extinction, not that there is none! The resulting mean value of the extinction is 2.5 mag with a peak value of 3.6 mag. From the map in Fig. 7c it becomes clear that the K' extinction towards most of the detected point sources has a value of about 2.5 mag. The extinction values at the positions of the point sources are used to de-redden their colours and thus to determine their spectral types in the next section.

4.2. Point sources

In 1989, Wood & Churchwell wrote in their fundamental paper on UCH II regions: "Multiple ionizing stars are clearly producing the UCH II region complexes we have seen, and it is possible that close binaries or clusters of young stars are responsible for ionizing individual UCH II regions as well... If the Trapezium were at a distance of 5kpc, its angular diameter would be only 1.8″, comparable to the size of many UCH II regions." Now it turns out that this was indeed a prophetic remark. The resolution of our AO images reveals for the first time that G45 contains more than a dozen single compact sources.

4.2.1. Sources inside the VLA map

In the deconvolved K' image shown in Fig. 3, we labelled 15 point sources inside the VLA map, which is superimposed as contours in the figure, with letters from a to o. Table 2 gives the results of the photometric measurements of these sources.

To confirm the presumed stellar nature of these point sources, we looked at their locations in a colour-magnitude diagram. Such a diagram is shown in Fig. 8. For comparison, a zero-age main sequence (ZAMS) as it would appear at a distance of 6.6 kpc is also shown. The grey shaded area denotes the track for reddening by interstellar dust grains after Rieke & Lebofsky (1985). It is clearly visible that the reddening track allows the sources to be ZAMS stars of spectral types O to B. To perform a further check on the nature of these unresolved sources, we used the measured K'-extinction values from Fig. 7c to de-redden the detected point sources. Combining these extinction values with the reddening vector from Rieke & Lebofsky (1985) results in the locations marked with primed letters in the diagram. Some remarks have to be made concerning this result:
First, most of the the de-reddened sources are still not on the ZAMS. Several reasons might be responsible for this result.

- The Brγ emission probably does not arise at the exact locations of the stellar sources but rather from the surrounding nebula. Thus, additional extinction from circumstellar dust might lead to more reddening than deduced from the Brγ extinction.
- Infrared excess emission, presumably from surrounding material might provide for a shift from the ZAMS.
- Contrary to radio photons, the Brγ photons are subject to scattering caused by dust particles. This mechanism might provide more Brγ photons in the line of sight than would have been detected in the absence of dust, again the extinction will be underestimated by the Brγ measurement (De Pree et al. 1994). To reduce this error in the future, polarization maps will have to be obtained, these can provide additional information on the scattering of the Brγ photons.

Second, the error bars are relatively large. The main error contributions come from the uncertainty of the predicted and the measured Brγ flux. We assume a flux error of $\pm$25% in the corrected 6 cm flux and thus almost the same in the predicted Brγ flux. Together with the high noise in the Brγ image from the continuum subtraction and calibration uncertainties, we get an extinction uncertainty of $\pm$0.44 mag. In total, we note that de-reddening the sources confirms their nature as high-mass ZAMS stars with the restriction that additional sources of extinction may exist that are not measured by the Brγ method and that uncertainties are fairly large.

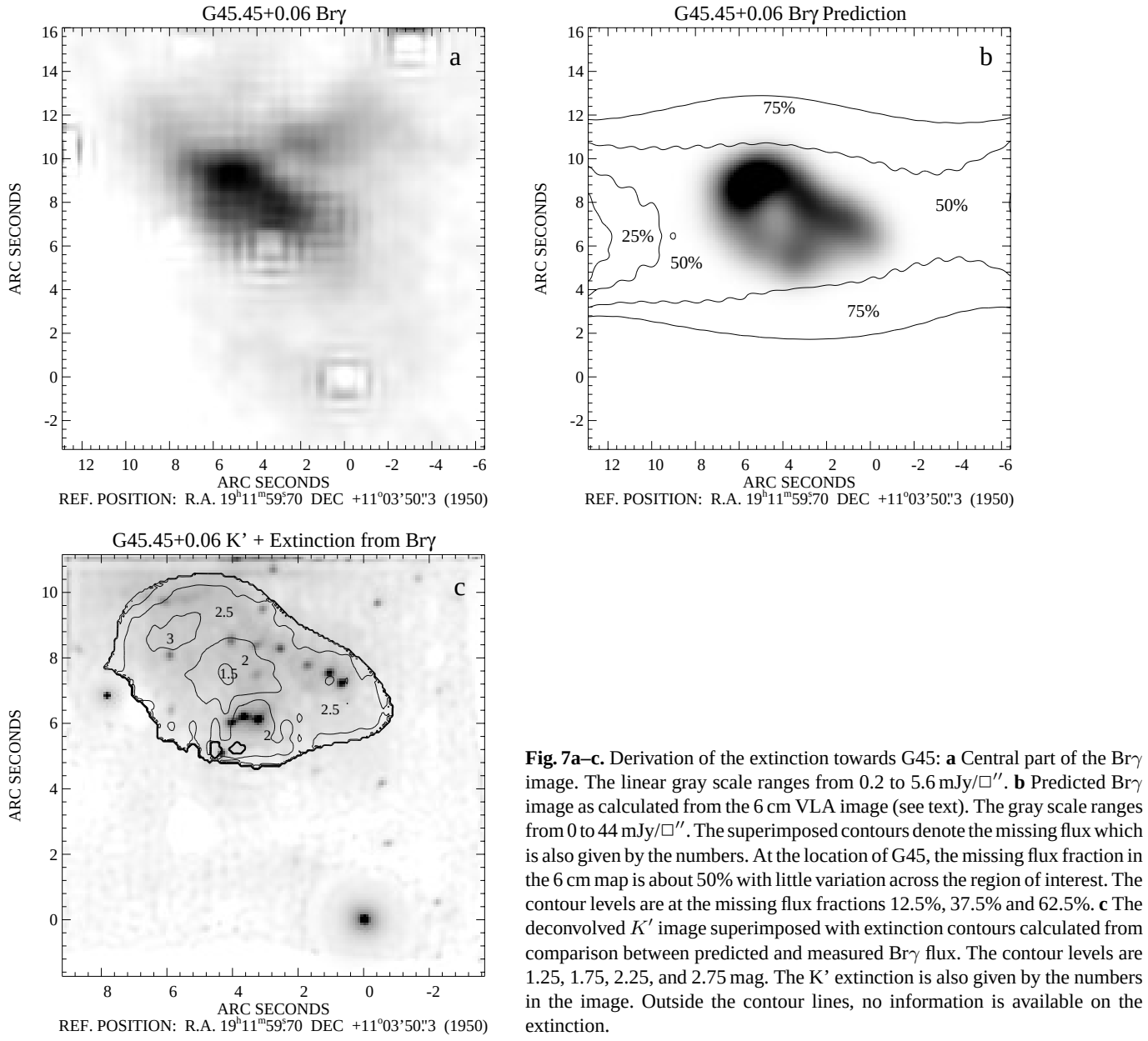

Fig. 7a–c. Derivation of the extinction towards G45: **a** Central part of the Brγ image. The linear gray scale ranges from 0.2 to 5.6 mJy/□″. **b** Predicted Brγ image as calculated from the 6 cm VLA image (see text). The gray scale ranges from 0 to 44 mJy/□″. The superimposed contours denote the missing flux which is also given by the numbers. At the location of G45, the missing flux fraction in the 6 cm map is about 50% with little variation across the region of interest. The contour levels are at the missing flux fractions 12.5%, 37.5% and 62.5%. **c** The deconvolved K' image superimposed with extinction contours calculated from comparison between predicted and measured Brγ flux. The contour levels are 1.25, 1.75, 2.25, and 2.75 mag. The K' extinction is also given by the numbers in the image. Outside the contour lines, no information is available on the extinction.

4.2.2. Other point sources

Two even more interesting sources are revealed by taking a look at the MIR images in Fig. 5: All show the strong point source *MIR1* at position (+3″,+10.″5). No trace of this source is found in the H image. Its spectral energy distribution is shown as the lower line in Fig. 6. We believe that this source is one of the youngest within the G45 complex; This issue is discussed in Sect. 4.5.

Another, weaker point source (*MIR2*) is visible at position (+3.″8,+4.″8). From the superimposed radio contours in Fig. 5 it becomes clear that the 10 and 12 μm position of this source is coincident with a radio peak, while it appears shifted by 0.″5 to the west at 3.5 μm. Additionally, there are 4 NIR point sources grouped along the northeastern side of this formation at a distance of approximately 1″ which corresponds to 6600 AU. Such positional shifts between wavelengths can be caused by surrounding dust or even a disk (see, e.g. Feldt et al. 1998 on Cha IRN, Stecklum et al. 1997 on GGD 27 or Close et al. 1997 on HL Tau). This object clearly *not* coincides with any NIR source.

Fig. 1 shows still more distinct sources, the two most interesting ones being the two mentioned before with the extended features attached to them at the positions (+4″,+10.″8) and (+6″,+9.″8) north of the chain-like arc. The extensions might be due to outflow phenomena, but for a save identification, high-resolution narrow-band images (H_2 2–1 (S1)) which trace the shocked molecular gas are needed. A first criterion in this direction would be the non-detection in our narrow band NIR images, which is the case at least for the object (+6″,+9.″8). At the other location, the resolution of the Brγ and its accompanying con-

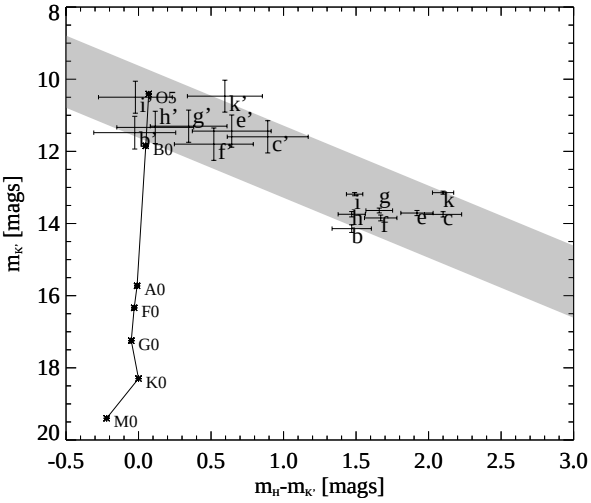

Fig. 8. Colour-magnitude diagram of the identified point sources. The error bars with unprimed letters denote the sources inside the VLA map of G45, the shaded area indicates the possible reddening tracks (after Rieke & Lebofsky 1985), crossing the region of the point sources. The solid line connecting the stars is the zero-age main sequence (ZAMS) at a distance of 6.6 kpc (From Straizys 1995). The error bars with primed letters denote the positions of the point sources after de-reddening. The K'-extinction used for this process is shown in Fig. 7C, the reddening vector is the same as denoted by the border of the grey shaded area.

tinuum image does not permit to decide where the extended emission in these images originates.

4.2.3. A young cluster?

As described in the preceding sections, most of the described point sources seem to be of stellar nature and thus to be young, massive stars. Their young age is generally indicated by the strong reddening or sometimes by attached extended features. Additional point sources can be seen in the VLA map shown in Fig. 3. The radio peaks are usually not coincident with NIR or MIR sources. Testi et al. (1997) have proposed an evolutionary sequence to explain that very young massive stars may not be visible at radio wavelengths, because their radio continuum is too much self-absorbed. Molinari et al. (1998) give the high mass infall rates at early stages of the massive star's life as a quenching mechanism for the radio emission.

However, the radio peaks are generally located close to NIR sources, which might indicate that they trace dense clumps of material which is ionized by the surrounding (young, massive) stars. They might even be identified as proplyd-like objects inside G45. Such disks around low-mass stars that are being ionized by nearby massive stars (see, e.g. McCullough et al. 1995 for an overview on the phenomenon) often exhibit some features of UCH IIs themselves (see, e.g. Stecklum et al. 1998 on G5.97-1.17). While the detection of G5.97-1.17 would not have been possible at the distance of G45 within the WC89 sample due to sensitivity constraints, a brighter proplyd might well be detected. Given the shorter projected distances inside G45 of only 1300 AU between source a and its neighbouring radio peak (G5.97-1.17 is at 4900 AU projected distance from Her 36), the larger distance towards the observer can be compensated and we can expect comparable beam brightness temperatures for the radio peak in G45 and for G5.97+1.17. Of course, this requires similar properties of the two systems, like density and size of the evaporating structure. Actually, the brightness temperature of the peak north of source a is 2300 K and that of the source south of l, m, and n is 3500 K, while that of G5.97+1.17 is only 1500 K. Assuming the required similar properties of the evaporating structures, source a has to be of slightly earlier spectral type than Her 36 (Stecklum et al. 1998 follow Woolf 1961 in their assumption that Her 36 is of spectral type O7) to the additional Lyman continuum flux for the higher measured beam brightness temperature. We do not have any information about the extinction towards a, but its non-detection in H renders such a spectral type improbable. Sources l, m, n, and o might easily provide enough photon flux to ionize a region of high density gas and thus be responsible for the radio peak 0.″8 southwest of them. Note that this object also appears as a thermal infrared source in the MIR images. In conclusion, we can not determine whether the radio peaks are ionized by the surrounding stars or internally or both, but all three possibilities clearly exist.

From the colour-magnitude diagram, we only have identified massive stars. We can estimate the range of the ZAMS we can cover with our method from the detection limit of $m_{K'} = 17.5$ mag and $m_H = 18.5$ mag. Assuming a mean extinction of 2.5 mag in K' and thus 4.0 mag in H for our assumed reddening values, we would be able to detect and identify the entire range of O and B stars down to around B8. A glance at Fig. 8 confirms that our latest identified object b is of spectral type around B1. The fact that we do not see intermediate mass stars is striking, but does not exclude the presence of lower mass are present inside G45. Assuming coevality, such stars would of course be in an earlier stage of their development and thus probably not appear on the ZAMS. When we estimate the K' luminosity of pre-main sequence (PMS) stars from 0.4 to 2.5 solar masses at the age of 1Myr from D'Antona & Mazzitelli (1994) using the polynomial fit method from Meyer (1996), we expect a maximum apparent magnitude of $m_{K'} = 15.5$ for a PMS star of 2.5 $M_\odot$. This estimate takes into account only the interstellar extinction and reddening towards G45 from Neckel & Klare (1980). If such a star is located inside the VLA map region with its mean extinction of 2.5 mag in K', we are not able to detect it.

However, we do have some candidate objects that possibly represent stars in an earlier evolutionary stage than the ZAMS. The first one is object *MIR1*, which is by far the most luminous MIR source. From Fig. 6 we learn that it contributes 10% of G45's infrared flux alone. It does not have a radio counterpart on the 6 cm map, but it is clearly visible in the new VLA map taken at 1.3 cm by Hofner et al. (1998). Also the two sources with the attached extended features might belong to the category of pre-ZAMS stars. As these sources at present are only detected in our high-resolution K-band image, their final identification will be the task of future studies of this region.

In general, none of the NIR sources show up in the mid-infrared images. From the sensitivities and resolutions of these images given in Table 1, this is what one would expect: Our brightest detected source, k, can be expected to be of m_L=11.8 mag and m_N=12.0 mag. For this estimate, we used the intrinsic colour indexes for an O5 star from Straizys (1995) and the reddening vector from Rieke & Lebofsky (1985). Although the source should show up in the L-band image, the large PSF-FWHM of this image prohibits the identification of single sources in this crowded field. Fig. 5 shows that MIR emission is highest close to the NIR point sources, whether this comes from the unresolved point sources themselves or from concentrations of warm dust cannot be decided from the data.

Overall, G45 seems to consist of the bright NIR sources close to a radio and MIR source at the southern edge, the chain of identified O- and B-stars along the radio ionization front and a couple of sources in an earlier phase of their evolution to the north. The linear distances fit that of massive star formation sites in our vicinity. From our biased sampling of the mass range it seems not unlikely that the initial mass function of this cluster extends towards lower mass stars which we are unable to identify at present.

4.3. The nebula

In this section, we will discuss the large scale morphological properties of the ionization nebula of G45. The large-scale structure of G45 is best visible in Fig. 4. Here, the Brγ emission comes from a shell-like structure with an additional arm stretching to the north. The ultracompact H II region G45 itself forms only the small, central part of this structure. This result is absolutely consistent with the findings of Garay et al. (1993) and W96, whose VLA image exhibits the same structure. As G45 is only a part of the shell-like structure, a closer look at its environment becomes necessary.

From the spherical shape and the large size of the ionized area, one might be tempted to conclude that G45 was not the primary cause for its ionization. Several possible sources of the large scale ionization provided by an external source can be thought of:

1. A supernova explosion at the centre of the shell. The expanding shock front might have triggered the formation of stars where it hit dense material. The shell-like structure as well as the arrangement of the newly formed stars in chains could well be explained by such a phenomenon (See, e.g. Gaensler et al. 1998 on G296.8-00.3, their source is comparable to G45 in distance, size and shape and Kothes et al. 1998 on G182.4+04.3). On the other hand, neither X-ray emission nor any other signpost of a supernova remnant is found close to G45 which rules out the supernova hypothesis.
2. W96 describe the cloud core associated with G45.47+0.05 as clumpy and fragmented from their HCO^+(1–0) measurements. A fragmenting process on a larger scale might have led to the development of a molecular cloud, the outside of which is now being ionized by an external source. If this was indeed the case, we should see the part of the cloud's rim ionized that is facing the ionization source. This scenario is very well matched by the horseshoe appearance of the ionized structure. A similar structure is found for NGC 3660 (Nürnberger priv. comm.) or in M16 (Pound 1998, Hester et al. 1996). Indeed, this would also indicate that G45 itself at the horseshoe's centre is closest to the source of ionization and therefore star formation is triggered in there first. Another hint towards the cloud hypothesis is that the 10 μm emission, which traces warm dust, follows the ionization front almost exactly. In Fig. 5b, it can be seen that the broad-band N image even traces a part of the larger shell structure. As the same morphology also shows up in the Brγ line, this results in a constant appearance of the source over more than 4 magnitudes of wavelengths, which makes foreground extinction an unlikely cause for its shape. Unfortunately, no bright source is visible close to G45 which could externally provide for its ionization. Therefore, we have to rule out this explanation as well.

Now that we have rejected the possibilities that a non-associated source is responsible for the ionization and thus for the formation of G45, we have to take a closer look at the internal energy budget. Later on we will draw a sketch of the formation of G45 which does not require any external influence. Even the large shell provides a radio flux of only 3.7 Jy at 3.6 cm according to W96. Using Kurtz, Churchwell, and Wood's (1994) estimate of the necessary rate of Lyman UV photons to provide the ionization for this flux, we get a rate of $10^{49.1}$ s^{-1}. According to model calculations by Panagia (1973), this rate can be provided by a single O6 star. Even at our adopted distance of 6.6 kpc and the corrected radio flux of 7.4 Jy, the required flux of $10^{49.5}$ s^{-1} ionizing photons per second can be provided by a single star of spectral type O5.5 ZAMS. In the absence of errors other than those of our photometry, our determination of spectral types from the colour indices plotted in Fig. 8 yields that source k should easily be able to provide the ionizing Lyman flux alone. Consequently, the energy budget of the shell structure does not require any ionizing source other than the stars we already see.

4.4. The role of dust in UCH II*s*

All these estimates were made in the absence of significant absorption of UV photons by dust. However, the MIR maps do show that at 10 μm the extended emission follows very well the ionization as seen in the radio map (see Fig. 5). Especially the 12 μm image, which does not contain the Ne II line proves that this is due to warm dust as noted above. Of course this is what one would expect, as the UV photons that ionize the gas also tend to heat up the dust grains - if a sufficient number of such grains exist. At 3.5 μm, the correlation between radio and MIR emission is less obvious. The differences in the distribution of the emission between the three MIR maps might well be explained by temperature effects. Additionally, these images

prove that the distribution of hot dusts also appears clumpy and irregular with a concentration along the ionization front.

To estimate the amount of UV absorption, we first determine the dust mass from our measured 12 μm flux by using

$$M_d = \frac{F_\nu d^2 c^2}{2h\nu^3}\left[e^{\frac{h\nu}{kT}}-1\right]\frac{1}{\kappa_\nu} \quad (7)$$

and the gas density by using

$$N_e = \sqrt{EM\frac{4}{\pi R}} \quad (8)$$

Eq. (8) uses the mean emission measure $EM = 3\times10^7$ pc cm^{-6}and assumes G45's shape as a half sphere with radius $R = 32000$ AU to determine the average gas density. The factor $\frac{4}{\pi}$ represents the conversion to the mean radius of the half sphere. This results in an electron density of 1.2×10^4 cm^{-3}, which is assumed to be equal to the gas density. Here, we use $F_\nu = 27.7$ Jy from our 12 μm image inside an aperture of 11″ diameter, $d = 6600$ pc, $\nu = 25.6$ THz as source dependent constants. κ is interpolated from Ossenkopf & Henning (1994) to be roughly 2.4×10^2 m^{2}kg^{-1} for 11.7 μm and the determined gas density of 1.2×10^4 cm^3. k is the Boltzmann constant, c the speed of light and h the Planck constant. For a temperature of 100 K we derive a dust mass of 0.02 M$_\odot$. Two remarks have to be made concerning this result: Firstly, the above formula assumes that the emission is optically thin - which should be the case at 12 μm if any UV photons get through the dust to provide ionization - which is obviously the case. However, the IRAS spectra show that this wavelength is still inside a broad absorption feature (see below), thus the derived mass is more a lower limit than an actual determination. Secondly, the result *strongly* depends on the dust temperature, therefore even this lower limit is a very crude estimate. Using this estimate together with

$$\tau_K = \kappa_K \rho_{dust} L \quad (9)$$

where κ_K is again taken from Ossenkopf & Henning (1994), this time for 2.15 μm, ρ_{dust} is the total mass of dust divided by the volume of the assumed half-sphere, and L the length of the line of sight through the absorbing matter (i.e. in this case equal to R), we determine a K optical depth of $\tau_K = 0.35$ or $A_K \approx 0.4$ mag. This converts into a UV extinction of $A_{0.09\mu\mathrm{m}} \approx 18$ mag after Mathis (1990). This result is checked against Ryter's (1996)

$$A_K = \frac{3.11N(H)}{4.93\times10^{21}\mathrm{cm}^{-2}\mathrm{mag}^{-1}}0.107, \quad (10)$$

where the last factor represents the conversion from A_V to A_K after Mathis (1990). Using the gas density from above as Hydrogen density and converting it to a column density by multiplying with the radius of our half-sphere, we also determine $A_K \approx 0.4$ mag. We note, that the latter method assumes a gas-to-dust-ratio of 100, while our mass estimates from above using the dust temperature of 100 K delivers a gas mass of 2.3 M$_\odot$ (also assuming a pure Hydrogen gas) and thus a gas-to-dust-ratio 111. This good agreement may serve as further justification for the crude estimate we introduced in the guess of the temperature.

Of course a UV extinction of $A_{0.09\mu\mathrm{m}} \approx 18$ would mean that almost no UV photons are available for ionization, but as we have detected at least 15 stars inside G45 and may assume that they are all (not only the identified eight) able to deliver sufficient ionizing flux, each of them only has to supply ionization in $\frac{1}{15}$ of the volume. Assuming spherical geometries, this results in a reduction of the radius of the spheres ionized by individual components and thus the extinction suffered by photons while travelling through these spheres by $\frac{1}{\sqrt[3]{15}}$ to $A_{0.09\mu\mathrm{m}} \approx 7.3$. After Aannestad (1989), this means that still more than 99% of all UV photons are absorbed before they can provide sufficient ionization. Thus, even our 15 stars (if they all are hot stars like the identified eight) cannot provide sufficient UV flux to ionize the region. We note, that 15 O5 stars would provide a total luminosity of 313×10^4 L$_\odot$. This is much more than the 144×10^4 L$_\odot$ measured by WC89 from IRAS data which translate to 66×10^4 L$_\odot$ at our distance of 6.6 kpc. Thus, some of the stars have to be of later spectral types, diminishing the UV photon flux even further. To get out of this dilemma, which underlines the importance of dust inside this kind of regions, we have to speculate about the distribution of dust inside the H II region. Although our MIR images cannot resolve it, the clumpy appearance of the MIR emission is visible in Fig. 5. Varying optical depths inside G45 could thus provide enough free paths for the ionizing photons to escape and ionize the surrounding gas.

We note that the result derived above also means, that our measured Brγ extinction largely is due to foreground dust. The additional internal extinction of A$_K \approx 0.4$ mag towards the centre of the cluster shifts our stars in Fig. 8 even more towards the ZAMS. However, we do not know, which stars are embedded how deeply, therefore we do not correct for this additional extinction in Fig. 8. The interstellar extinction towards G45 should only amount to A$_{K,interstellar} \approx 0.7$ mag according to Neckel & Klare (1980) and Mathis (1990) while we have measured 2.8 mag towards the ionized region. from the comparison to A$_K \approx 0.4$ mag *inside* G45, we can derive that the major fraction of (cold, i.e. invisible in the MIR) dust is situated between us and the source. A similar scenario is assumed for the Orion Trapezium Cluster, where the O stars are thought to have have cleared a bubble in the surrounding dust (Felli et al. 1993).

Unfortunately, the three MIR images are of significantly different quality in terms of resolution and sensitivity. This renders quantitative statements on the dust temperature or optical depths of possible silicate features very difficult and thus we will not try to make one. The IRAS LRS spectrum of the source does show a pronounced absorption feature between 8 and 12.5 μm, but its centre wavelength is close to 11 μm, untypical for a (pure) silicate feature. As this feature comprises almost our entire N band filter, we decided it would be of little use to compare the 11.7 μm image and the N-band image to derive an optical depth. Also the wavelength base is very short between 10.5 μm and 11.7 μm, especially as 11.7 μm still is within the absorption feature. Additionally, it has to be marked, that the large IRAS beam probably measured the total of G45.45+0.06. Thus, without further infor-

mation on the SED in this part of the spectrum, we will refrain from statements on temperature and optical depth.

4.5. The nature and history of G45

One of the original goals of our investigations was to identify and classify the ionizing source of G45. However, during the previous sections it has become clear that this is a very difficult task. On the one hand, it is not immediately obvious if G45 is internally ionized at all, on the other hand we did not find *the* strong point source that coincides in position at all the observed wavelengths like e.g. Watson et al. (1998) claim to have identified in G29.96-0.02.

In the previous section we ruled out the possibilities of external ionization for reasons of the energy budget, which does not require any ionizing flux other than that from the stars inside G45 (except for the dust problem), and because no traces of possible ionizing sources like supernovae or clusters of OB stars can be found in reasonable vicinity to G45.

We will now try to draw a complete while still coarsely simplified picture of "G45 - The Orion nebula's younger brother". For an extensive review on the Orion regions see e.g. Genzel & Stutzki 1989 and Felli et al. 1993.

The stars labelled $o, l, m,$ and n are situated close to a radio point source as well as to a clump visible in the mid-infrared. Although the flux from $l, m,$ and n can not be measured due to their small separation in the un-deconvolved image, they belong to the brightest sources in the field. Therefore and for reasons explained below, we believe that star formation in G45 had its origin here. Massive stellar winds and the expanding ionization front swept through the ambient matter and formed the structure we see today.

The morphology of the radio shell can be explained by means of density gradients in the molecular material. The expansion towards the southeast happened faster and did not create visible star formation sites. In contrast, the ionization front seems to have hit dense clumps of material to the north, creating the cometary structure of G45 and triggering sequential star formation in dense and/or already collapsing molecular cloud cores. The result of this procedure is now visible as the chain of ZAMS-stars grouped along the ionization front. Unfortunately, there are no high-resolution maps at wavelengths that trace the distribution of cold dust to confirm our hypothesis. The 1.3 mm map of Mooney et al. (1995) shows an almost spherically symmetric distribution around the position of G45 at a resolution of $12''$. This resolution is of course too low do detect any details on scales that are visible in our NIR images and the VLA maps.

North of the ionization front as visible in Fig. 3, we detect several sources that show characteristics of stars in an evolutionary phase earlier than the ZAMS. The most obvious of these is source *MIR1* which exhibits very strong MIR emission and provides approximately 10% of the infrared luminosity of G45. The spectral index of this object with $a = \frac{d(\log(\lambda F_\lambda))}{d\log(\lambda)} \approx 4.5$ between 2.2 and 12 μm would qualify this object for Lada class I following Wilking et al. 1989. At least two more objects with extended features are visible north of the front in Fig. 1. All of these objects need to undergo further examinations to determine their nature.

The apparent distances between the single point sources range from $0\farcs4$ to about $2''$. At the adopted distance of 6.6 kpc, this implies projected physical distances of around 2600 AU to 13000 AU. This distance range fits very well that of the central part of the Orion nebula around the Trapezium region, another hint that G45 may be a young twin of that region in the making.

The surroundings of G45 which include the UCH IIs G45.48+0.13 and G45.47+0.05 appear clumpy and fragmented on a larger scale (W96). The latter authors also speculate on triggered formation of UCH IIs which had its origin at G45, because it is the most evolved UCH II in the region.

Drawing the parallel to the Orion region, we would identify the stars o, l, m, and n as our Trapezium cluster where it all started. The necklace along the ionization front with its extended emission of NIR and MIR light would then be an analogue of the KL region, with several young massive stars embedded in the local concentrations of hot dust. While in Orion not all embedded point sources have been identified as self-luminous YSOs (Genzel & Stutzki 1989), all our sources that could be identified turned out to be young massive stars.

These most probably have been formed as a consequence of the ionization and shock front passing through these clumps. North of that front, source *MIR1* might even be an analogue of the BN object, although its nature is much more uncertain up to now than that of BN. On the large scale, the younger UCH IIs at distances around 57 pc might then be counterparts for the other OB associations in the Orion region which are located at comparable distances from the Trapezium and KL/BN. In Orion, the other OB associations are believed to be older than the Trapezium cluster while G45 itself is believed to be the oldest and most evolved UCH II in the Region (W96 on G45 and Genzel & Stutzki 1989 on Orion). W96 speculate on G45 having triggered star formation in the other UCH IIs nearby - a scenario which has been introduced by Elmegreen & Lada (1977).

This parallel is another strong evidence that the formation of massive stars usually happens in clusters and leads to induced star formation in its vicinity. With the new techniques of high resolution imaging, it is now possible to enlarge the sample of these massive star formation sites towards more distant objects. Our example of G45 proved that this enlargement includes the detection of objects in an earlier phase of their evolution than the Orion region. More examples of the benefits of these high-resolution imaging techniques applied to massive star formation sites will be added in the near future.

5. Conclusions

In this paper, we presented new observational data on G45, covering the near- and mid-infrared wavelengths. On our K' and H band images taken with the adaptive optics system ADONIS, we detected several point sources eight of which could be identified as O and B stars from colour-magnitude measurements. This identification was only made possible by the extraordi-

nary resolution of 0.″4 provided by the adaptive optics. These identifications were checked against measurements of the extinction towards G45. The extinction was calculated from the comparison of our measured Brγ flux and the prediction for Brγ emission from 6 cm VLA maps. Additional extinction was found from a determination of the dust mass inside G45 from our MIR images. The derived high optical depths inside the region pose a significant problem for ionization by UV photons if the matter is distributed homogeneously inside G45. On our mid-infrared images, we detected two more sources which obviously represent young stellar objects. By combining these data, we argued that G45 is a young cluster of O- and B-stars similar to those being formed in the Orion regions in size but obviously younger and still in the formation process. Additionally, we argued on the history of star formation on the basis of an apparent age gradient from south (readily formed massive stars) to north (chain of stars along the ionization front and, further north, several objects either heavily reddened or with extended features). These findings confirm earlier speculations by WC89 on UCH IIs being young OB clusters, as well as of W96 on sequential star formation in the area triggered by G45. For the first time, we have brought up direct evidence that one form of UCH IIs is a cluster of massive stars. Our images suggest that sequential star formation does take place in these clusters.

Acknowledgements. We are indebted to D.O.S. Wood as well as to D.J. Wilner for supplying their VLA data in FITS format. Without these data, large parts of our work would not have been possible. B. Stecklum is grateful for P. Bouchet's help with the ADONIS system. Also, M. Feldt acknowledges the invaluable assistance of M. Robberto and M. Gai during the observations at the TIRGO telescope. M. Feldt is being funded by the Max-Planck-Society, Germany. R. Klein is funded by grant No. 50 OR 9414 9 of *BMBF Verbundforschung fürAstronomie/Astrophysik* . We thank an anonymous referee for extensive comments which helped to greatly improve the paper.

References

Aannestad P.A., 1989, ApJ 338, 162
Baud B., 1976, A&A 57, 443
Becklin E.E., Neugebauer G., 1967, ApJ 147, 799
Beuzit J.L., Hubin N., Gendron E., et al., 1994. In: Proc. SPIE 2201, "Adaptive Optics in Astronomy", p.955
Böker T., Storey J.W.V., Krabbe A., Lehmann Th., 1997, PASP 109, 827
Brand J., 1986, PhD Thesis, Leiden Univ. (Netherlands)
Brand J., Blitz L., 1993, A&A 275, 67
Churchwell E., Felli M., Wood D. O. S., Massi M. 1987, ApJ 321, 516
Churchwell E., Walmsley C.M., Cesaroni R., 1990, ApJS 83, 119
Churchwell E., 1991, in: Lada C., Kylafis, N. (eds.) The Physics of Star Formation and Early Stellar Evolution, Kluwer, Dordrecht, p.221
Close L.M., Laird M., Roddier F. et al., 1997, ApJ 478, 766
D'Antona F., Mazzitelli I., 1994, ApJS 90, 467
Elmegreen B.G., Lada C.J., 1977, ApJ 214, 725
Feldt M., Henning Th., Lagage P.O., et al., 1998, A&A 332, 849
Felli M., Churchwell E., Wilson T.L., Taylor G.B., 1993, AAS 98, 137
Gaensler B. M., Manchester R. N., Green A. J. 1998, MNRAS 296, 813
Garay G., Rodriguez L.F., Moran J.M., Churchwell E., 1993, ApJ 418, 368
Genzel R., Stutzki J., 1989, ARA&A 27, 41
Hayward T. L., Miles J. W., Houck J. R., Gull G. E., Schoenwald J. 1993, Proc. SPIE, 1946, 334
Henning Th., 1990, Fundamentals of Cosmic Physics 14, 321
Herbst T.M., Beckwith S.V.W., Birk Ch., et al., 1993, In: Proc. SPIE 1946, "Infrared Detectors and Instrumentation", p 605
Hester J. J., Scowen P. A., Sankrit, R, et al., 1996, AJ 111, 2349
Hofner P., Peterson S., Cesaroni R., 1998, ApJ, submitted
Hollenbach D., Johnstone D., Lizano S., Shu F., 1994, ApJ 428, 654
Howard E.M., Pipher J.L., Forrest W. J. 1994, ApJ 425, 707
Hummer D.G., Storey P.J., 1987, MNRAS 224, 801
Kleinmann D.E., Low F.J., 1967, ApJL 149, L1
Kothes R., Furst E., Reich W., 1998, A&A 331, 661
Kurtz S., Churchwell E., Wood, D.O.S, 1994, ApJS 91, 659
Lucy L.B. 1974, AJ, 79, 745
Mathis J. S., 1990, ARA&A 28, 37
Matthews H.E., Goss W.M., Winnberg A., Habing H.J., 1977, A&A 61, 261
McCullough P. R., Fugate R. Q., Christou J. C., et al., 1995, ApJ 438, 394
Meyer M.R., 1996, Ph.D. Thesis, University of Massachusetts, Amherst
Mezger P.G., Henderson A.P., 1967, ApJ 147, 471
Molinari S., Brand J., Cesaroni R., Palla F., Palumbo G.G.C., 1998, A&A, in press
Mooney T., Sievers A., Mezger P.G., et al., 1995, A&A 299, 869
Neckel Th., Klare G., 1980, A&AS 42, 251
O'Dell C. R., Wen Z., 1994, ApJ 436, 194
Osterbrock D. E., 1989, Astrophysics of Gaseous Nebulae and Active Galactic Nuclei, Mill Valley, California, Univ. Science Books
Ossenkopf V., Henning Th, 1994, A&A 291, 943
Pantin E., Starck J.L., 1995, A&AS 118, 575
Panagia N., 1973, AJ 78, 929
Persi P., Felli M., Lagage P.O., Roth M., Testi L., 1997, A&A 327, 299
Pound M.W., 1998, ApJL 493, 113
Rieke G.H., Lebofsky M.J., 1985, AJ 288, 618
Robberto M., Gai M., Guarnieri M. D., et al., 1994, in: Crawford D.L., Craine E.R. (eds.), Instrumentation in Astronomy VIII, Proc. SPIE Vol. 2198, p. 446-456
Rohlfs K., 1990, Tools of Radio Astronomy, Heidelberg, Springer Verlag
Ryter Ch.E., 1996, ApSS 236, 285
Stecklum B., Hayward T.L., Feldt M., Löwe M., 1995, ESO Msngr 82, 16
Stecklum B., Feldt M., Richichi A., Calamai G., Lagage P.O., 1997, ApJ 479, 339
Stecklum B., Henning Th., Feldt M., et al., 1998, AJ 115, 767
Straizys V., 1995, Multicolor Stellar Photometry, Tucson, Arizona, Pachart Publishing House
Testi L., Felli M., Persi P., Roth M., 1997, A&A 329, 233
Van Buren D., MacLow M.M., Wood D.O.S, Churchwell E, 1990, ApJ 353, 570.
Watson A.M., Coil A.L., Sheperd D.S., Hofner P., Churchwell E., 1998, ApJ in press.
Wilking B.A., Lada C.J., Young E.T., 1989, ApJ 340, 823
Wilner D.J., Ho P.T.P., Zhang Q., 1996, ApJ 462, 339 (W96)
Wood D.O.S., Churchwell E., 1989, ApJS 69, 831 (WC89)
Woolf N. J., 1961, PASP 73, 206
Wynn-Williams C.G., Downes D., Wilson T.L., 1971, Astrophysical Letters 9, 113
Yorke H. W., Welz A., 1996, A&A 315, 555